

Crustal structure of the Western U.S. from Rayleigh and Love wave amplification data

William Sturgeon¹, Ana M.G. Ferreira^{1,2}, Lewis Schardong³, Augustin
Marignier^{1,4}

¹Department of Earth Sciences, Faculty of Mathematical & Physical Sciences, University College London,
WC1E 6BT, UK

²CERIS, Instituto Superior Técnico, Universidade de Lisboa, Av. Rovisco Pais 1, 1049-001 Lisboa,
Portugal

³The Geological Survey of Israel, Jerusalem, Israel

⁴Mullard Space Science Laboratory, University College London, RH5 6NT, UK

Key Points:

- We present SWUS-crust, a new crustal model of the western U.S.
- Love wave amplification measurements are used for the first time and are jointly inverted with Rayleigh wave amplification measurements.
- We image well-known features and sharpen others, such as beneath the High Lava Plains.

17 **Abstract**

18 We present SWUS-crust, a three-dimensional shear-wave velocity model of crustal struc-
 19 ture in the western U.S. We use Rayleigh wave amplification measurements in the pe-
 20 riod range of 38–114 s, along with Love wave amplification measurements in the period
 21 range of 38–62 s, with the latter being inverted for the first time for crustal velocity struc-
 22 ture. Amplification measurements have narrower depth sensitivity when compared to
 23 more traditional seismic observables such as surface wave dispersion measurements. In
 24 particular, we take advantage of the strong sensitivity of Love wave amplification mea-
 25 surements to the crust. We invert over 6,400 multi-frequency measurements using the
 26 Monte-Carlo based Neighbourhood Algorithm, which allows for uncertainty quantifica-
 27 tion. SWUS-crust confirms several features observed in previous models, such as high-
 28 velocity anomalies beneath the Columbia basin and low-velocity anomalies beneath the
 29 Basin and Range province. Certain features are sharpened in our model, such as the north-
 30 ern border of the High-Lava Plains in southern Oregon in the middle crust.

31 **Plain Language Summary**

32 When an earthquake ruptures, seismic surface waves called Rayleigh and Love waves
 33 travel along the Earth's surface. Seismometers on the Earth's surface record ground mo-
 34 tions caused by the passing seismic waves. The amplitude of these waves contains infor-
 35 mation about the local Earth structure beneath the station, from which we can produce
 36 images of the Earth's interior. Whilst Rayleigh waves have previously been used to im-
 37 age the Earth's upper mantle, this study represents the first time that Love waves have
 38 been used, resulting in a new crustal model of the western U.S., called SWUS-crust. The
 39 model correlates with many well-known surface tectonic features, such as the Columbia
 40 Basin, Basin & Range province and Colorado Plateau. We also highlight certain features
 41 that have not been seen clearly in previous models, such as the High-Lava Plains in south-
 42 ern Oregon.

43 **1 Introduction**

44 Seismic imaging plays a crucial role in probing the structure and composition of
 45 the Earth's crust, especially when combined with laboratory measurements of crustal
 46 rocks (e.g., Christensen & Mooney, 1995; Rudnick & Gao, 2014). Seismic images of the
 47 Earth's crust are also useful for seismic hazard assessment (e.g., by providing key input

48 information for accurate ground motion simulations) and are crucial for accurate earth-
49 quake source modelling (e.g., Frietsch et al., 2021). Moreover, removing the effects of the
50 heterogeneous crust on seismic measurements can help constrain mantle structure (e.g.,
51 Ferreira et al., 2010; Schaeffer & Lebedev, 2015).

52 There are several global models of the crust, including CRUST1.0 (Laske et al., 2012),
53 LITHO1.0 (Pasyanos et al., 2014) and the more recent model of Szwilus et al. (2019).
54 These models constrain crustal seismic velocities on a $1^\circ \times 1^\circ$ grid scale and are mainly
55 based on compilations of existing seismic and geophysical information, as well as on the
56 modelling of seismic data. However, higher resolution models can be achieved on a re-
57 gional scale. The dense network of EarthScope's USArray, which ended in 2021 (<http://www.usarray.org/>),
58 provides an opportunity to image the local crust in finer detail across the continental U.S.
59 (e.g., Schmandt & Humphreys, 2011; Porter et al., 2016). In particular, the western U.S.
60 is an interesting study region due to its complex geological history and its wide range
61 of tectonic provinces.

62 Crustal thickening through tectonics across the western United States was largely
63 controlled by the subduction of the Farallon plate in the late Mesozoic and Cenozoic (e.g.,
64 Schellart et al., 2010). Progressive subduction over the past >150 Ma caused major tec-
65 tonic uplift and magmatism throughout the region (e.g., Humphreys & Coblenz, 2007).
66 In the Cretaceous, subduction of the Farallon plate produced volcanism in the crust, even-
67 tually forming the Sierra Nevada batholith (Bateman & Eaton, 1967). Later, the Laramide
68 orogeny is thought to have been responsible for crustal thickening and uplift of the Rocky
69 Mountains range and of the Colorado Plateau in the east, which remains largely unde-
70 formed since the early Cenozoic compression and extension (e.g., Tesauro et al., 2014).
71 Further north, subduction also formed the Cascade Mountain range through crustal thick-
72 ening, which is home to a belt of Quaternary volcanoes above the Juan de Fuca plate
73 subduction zone (Hildreth, 2007). In the Miocene, changes in the geometry of the Far-
74 allon slab led to extension and crustal thinning. The thinned crust of the North Basin
75 & Range (Huber, 1981) produced low elevations across the area (e.g., Braile et al., 1989)
76 and renewed volcanic activity (e.g., Stewart, 1980), but also increased elevations along
77 the Sierra Nevada mountain range. Further north, intense magmatism about 17 Ma formed
78 the Columbia Basin, a large igneous province caused by basaltic volcanism (e.g., Chris-
79 tiansen et al., 2002). Recent magmatism also marks the High Lava Plains (HLP in Fig-
80 ure 1) in south-eastern Oregon, the Snake River Plain (SRP in Figure 1) and the Yel-

81 lowstone hotspot. Given such complex tectonic evolution, overall the western US shows
82 a wide range of crustal structure, from thin crust in the Basin & Range (~ 25 km) and
83 along the Pacific border (~ 20 km), to intermediate crustal thickness values in the Columbia
84 Basin (~ 35 km) and thick crust beneath Rocky Mountains (~ 50 km) (Laske et al., 2013).

85 Many previous studies have utilised the large amount of available data from the
86 USAArray to image the crustal structure of the western U.S.. Surface wave ambient noise
87 tomography has been one of the most widely used techniques to image shear-wave ve-
88 locity in the crust (e.g., Shapiro et al., 2005; Bensen et al., 2009; Moschetti et al., 2007;
89 Lin et al., 2008; Schmandt et al., 2015; Xie et al., 2018; Porter et al., 2016). In addition
90 to ambient noise, receiver functions have also been commonly included to improve the
91 depth-resolution of crustal layers (e.g., Shen et al., 2013; Schmandt et al., 2015; Chai et
92 al., 2015). To further improve sensitivity to the crust, Rayleigh wave ellipticity measure-
93 ments have also been included in more recent studies (e.g., Shen & Ritzwoller, 2016; Lin
94 et al., 2014). Moreover, Pn waves (P waves trapped below the Moho) have also been used
95 to constrain crustal and uppermost mantle structure in the U.S. For example, Buehler
96 and Shearer (2012) used Pn measurements in the western US to estimate crustal thick-
97 ness variations and velocity perturbations just below the Moho. More recently, Tesauro
98 et al. (2014) used a variety of seismic data types, including Pn measurements, to con-
99 strain crustal depth, crustal P-wave velocity maps and Pn velocity maps beneath the U.S.

100 Another seismic observable that has recently received some attention is surface wave
101 amplification, which carries information on how surface wave amplitudes change due to
102 the local mantle and crustal structure at a given location (e.g., Eddy & Ekström, 2014).
103 Recent studies have shown that surface wave amplification measurements have the po-
104 tential for higher-resolution imaging when compared to surface wave dispersion measure-
105 ments (e.g., Eddy & Ekström, 2014; Schardong et al., 2019). Surface wave amplification
106 has been measured in a few studies. Taylor et al. (2009) measured site amplification fac-
107 tors using ambient noise in California using a standing-wave methodology. Later, Lin
108 et al. (2012) measured receiver-side amplification across the USAarray using fundamen-
109 tal mode Rayleigh waves with a method similar to Eikonal and Helmholtz tomography.
110 Eddy and Ekström (2014) developed a novel method to measure local amplification us-
111 ing amplitude ratios at nearby stations, which we will discuss in more detail later in this
112 study. Schardong et al. (2019) built upon the methodology of Eddy and Ekström (2014)
113 to generate a new dataset of amplification measurements across the western U.S. for vertical-

and horizontal-component Rayleigh waves and Love waves in the period range between $T \sim 38$ s and $T \sim 114$ s. This study was the first to invert amplification measurements for crustal and mantle shear-wave velocity structure in the western U.S. The resulting model, SWUS-amp, used vertical-component Rayleigh wave amplification measurements to constrain mantle shear-wave velocity down to ~ 300 km depth. However, the crust was only parameterised using a single layer between the Moho and surface since the data used could not constrain more complex crustal models (Figure S1).

In this study we combine Love and Rayleigh wave amplification measurements to constrain crustal shear-wave velocity in the western U.S. Love waves have a particularly strong sensitivity to crustal structure, which is explored in this work. The Love wave measurements are jointly inverted with Rayleigh wave amplification measurements to build 1-D shear-wave velocity models beneath each considered station in the western USAArray. Then, these 1-D profiles are interpolated to build a new 3-D shear-wave speed model of the crust, SWUS-crust. Finally, we interpret the features imaged in SWUS-crust and compare them to those reported in other recent studies.

2 Surface wave amplification measurements

2.1 Seismic data

We use fundamental-mode vertical-component Rayleigh (hereafter referred simply as Rayleigh waves) and Love wave amplitude anomalies. Both datasets were measured using the mode-branch stripping technique (van Heijst & Woodhouse, 1997). The Rayleigh wave dataset has also been used in global studies of attenuation (Bao et al., 2016; Dalton et al., 2017) and in the study of Schardong et al. (2019), which determined crustal and upper mantle shear-wave velocity beneath the western U.S. This dataset contains data from the Transportable Array, which was part of the larger USArray between 2004 to 2007. The dataset is based on 7,744 earthquakes with $M > 5.0$ that occurred in 2004-2007, recorded at 351 stations in the western U.S. Figure 1 shows the locations of the stations used in this study and their networks. Rayleigh waves are measured at 12 dominant periods between $T \sim 38$ -114 s, whereas Love waves are measured at seven dominant periods between $T \sim 38$ -62 s. We choose to include only shorter-period Love wave measurements ($T \leq 62$ s), which have stronger sensitivity to the crust, as can be seen in Figure S2. We performed inversions using longer-period Love waves ($T \sim 69$ -113 s), which

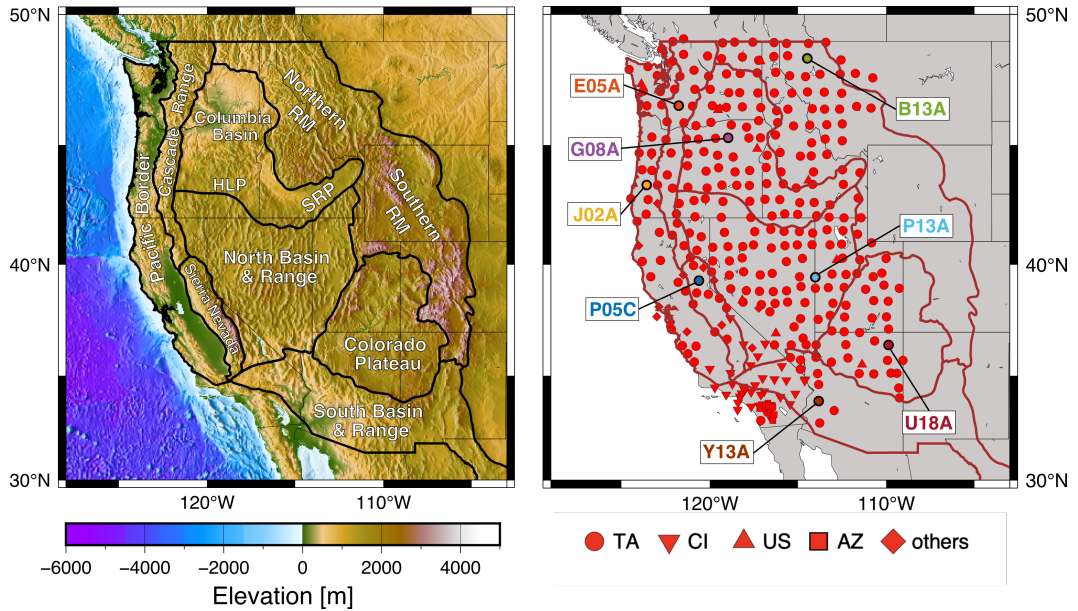


Figure 1. Left: Map of the western U.S., it's major tectonic provinces and other notable features, including the Rocky Mountains (RM), the Snake River Plain (SRP) and High Lava Plains (HLP). The elevation and bathymetry of the region are also plotted, according to ETOPO1. Right: the location of all 351 stations used in this study, with their network represented by different symbol types, as shown in the key. Other networks (diamond symbol) include BK, NN, IU, LB and LI. For each major tectonic province we selected one illustrative station, which is labelled. These eight selected stations are used as illustrative examples throughout this paper. The major tectonic provinces are delineated as solid brown lines.

145 resulted in very similar 1-D shear-wave speed (v_S) profiles in the crust, thus not affecting
 146 the results of this study, but they occasionally led to less stable inversions likely due
 147 to noisier measurements. Our measurement procedure provides a total of 6,423 multi-
 148 frequency, surface-wave amplification measurements used in this study.

149 **2.2 Measurement technique**

150 We use Rayleigh and Love wave amplification measurements obtained with the mea-
 151 surement technique developed by Schardong et al. (2019), which is briefly summarised
 152 in this section. The local frequency-dependent amplification of surface waves at a given
 153 receiver, R , is theoretically expressed by (e.g., Ferreira & Woodhouse, 2007):

$$A_R(\omega) = \frac{Y(\omega)}{Y_0(\omega)} \sqrt{\frac{C_g^0(\omega)}{C_g(\omega)}}, \quad (1)$$

154 where $Y(\omega)$ is the local displacement eigenfunction of the Earth's normal mode equiv-
 155 alent to the surface wave considered at a given frequency ω . $Y(\omega)$ corresponds to the
 156 vertical component eigenfunction $U(\omega)$ for Rayleigh waves, and to the transverse com-
 157 ponent eigenfunction $W(\omega)$ for Love waves. $C_g(\omega)$ is the local group velocity which is
 158 measured from spheroidal and toroidal modes for Rayleigh and Love waves, respectively.
 159 $Y_0(\omega)$ and $C_g^0(\omega)$ are the corresponding eigenfunction and group velocity, respectively,
 160 computed for the 1-D reference model PREM (Dziewonski & Anderson, 1981). The eigen-
 161 functions and group velocities are calculated using a normal mode formalism (F. Gilbert,
 162 1971) and using the software package Mineos 1.0.2 (Masters et al., 2011).

163 In addition to the amplification (or receiver) contribution $A_R(\omega)$, observed surface
 164 wave amplitudes are also affected by source and path effects. Eddy and Ekström (2014)
 165 developed a method to remove the contribution from the source and path by averaging
 166 ratios of amplitudes between pairs of nearby stations i and j , which is ideally suited to
 167 dense seismic networks such as the USArray. Local amplification, $d_{ij}^k(\omega)$, is calculated
 168 by taking the ratios of surface-wave amplitudes for a given earthquake, k :

$$d_{ij}^k(\omega) = \ln(A_i(\omega)/A_j(\omega)) = \ln(A_i(\omega)) - \ln(A_j(\omega)) \quad (2)$$

169 followed by an average taken over all the earthquakes considered. Schardong et al.
 170 (2019) followed the same approach, but with some minor modifications considering an
 171 azimuthal weighting of the earthquakes,

$$\bar{d}_{ij}(\omega) = \frac{\sum_{k=1}^{N_E} d_{ij}^k w^k}{\sum_{k=1}^{N_E} w^k} \quad (3)$$

172 The azimuthal weighting coefficient is given by $w^k = 1 - n_E/N_E$, where n_E is
 173 the number of earthquakes located in an azimuthal bin of 15° , for each earthquake k ,
 174 and N_E is the number of common earthquakes recorded at stations i and j . We then cal-
 175 culate the corresponding weighted standard deviation using:

$$\sigma_{ij}(\omega) = \sqrt{\frac{\sum_{k=1}^{N_E} w^k (d_{ij}^k(\omega) - \bar{d}_{ij}(\omega))^2}{\frac{N_E-1}{N_E} \sum_{k=1}^{N_E} w^k}} \quad (4)$$

176 We then invert the average inter-station frequency-dependent measurements for lo-
 177 cal amplification factors at each station ($A_{R,i}$ and $A_{R,j}$). Adopting a least-squares in-
 178 version approach, we minimise the misfit function:

$$m^2 = \sum_{ij} \frac{1}{\sigma_{ij}^2} [(\ln(A_{R,i}(\omega)) - \ln(A_{R,j}(\omega)) - \bar{d}_{ij}(\omega))^2] \quad (5)$$

179 To constrain the inversion, Schardong et al. (2019) imposed the condition that the
 180 sum of the amplification factors must equal the sum of the theoretical amplification fac-
 181 tors (Equation 1), calculated using SGLOBE-rani (Chang et al., 2015) for mantle struc-
 182 ture combined with CRUST2.0 (Bassin, 2000) for crustal structure.

183 It was noted in Schardong et al. (2019) that the amplification values obtained with
 184 distinct amplification sum constraints vary significantly, which would lead to distinct ab-
 185 solute v_S values when inverting the amplification measurements. Therefore, absolute val-
 186 ues of v_S will not be interpreted in this study. However, it was found that inverted v_S
 187 perturbations did not strongly depend on the imposed sum of the amplification factors,
 188 therefore our model can be interpreted in terms of v_S perturbations.

189 Inter-station measurement uncertainties, \mathbf{e}_R , are calculated at all stations and avail-
 190 able periods using:

$$\underline{\mathbf{e}}_R = \sqrt{\text{diag}(\underline{\mathbf{P}}^{-1} \cdot \underline{\mathbf{S}} \cdot (\underline{\mathbf{P}}^{-1})^T)} \quad (6)$$

where the \mathbf{P} matrix relates $\ln(A_{R,i}(\omega)) - \ln(A_{R,j}(\omega))$ with $d_{ij}(\omega)$ (Equation 5) and $\underline{\mathbf{S}}$ a diagonal matrix containing observed data uncertainties in the form of weighted standard deviations (Equation 4). These errors cannot be directly compared to previous studies (e.g., Lin et al., 2012; Eddy & Ekström, 2014) because of different data error definitions used.

We also apply selection criteria on our amplification curves in order to remove all outliers, for both Rayleigh and Love waves. Specific details are given in the supplementary information of Schardong et al. (2019), and here we briefly summarise them. As shown in Figure S3, we ensure that we only consider amplification factors for which five or more inter-station measurements are available. We ensure there is a good azimuthal coverage of stations around our primary station, in order to avoid azimuthal biases leaking into our inter-station amplification measurements. Specifically, we remove all stations with an azimuthal completeness coefficient of less than 20% (as defined by Equation 2 in the SI of Schardong et al., 2019). Outliers due to geographical coherency are removed by ensuring amplification factors for each station do not vary by more than 2.5σ compared to all nearby stations, where σ is the standard deviation of the amplification values of all nearby stations. Lastly, we remove all stations with a propagated error greater than 0.1, as given by Equation 6. This threshold value ensured obvious outliers were removed, whilst keeping the bulk amount of data available.

In this study we perform inversions of inter-station amplification measurements from 432 stations in the western U.S., which have both Rayleigh and Love amplification data. Following these inversions, we removed stations for which the inversions had a data misfit larger than 20 (Equation 7). Moreover, we visually examined all the stations and removed those that showed rough (i.e., non-smooth) or irregular amplification curves that could not be matched in the inversions. As a result, we kept a total of 351 stations and are still left with a good distribution of stations across the region (Figure 1).

2.3 Results

Figure 2 shows illustrative examples of observed amplification curves for Rayleigh and Love waves compared to theoretical predictions using the 1-D depth profiles from

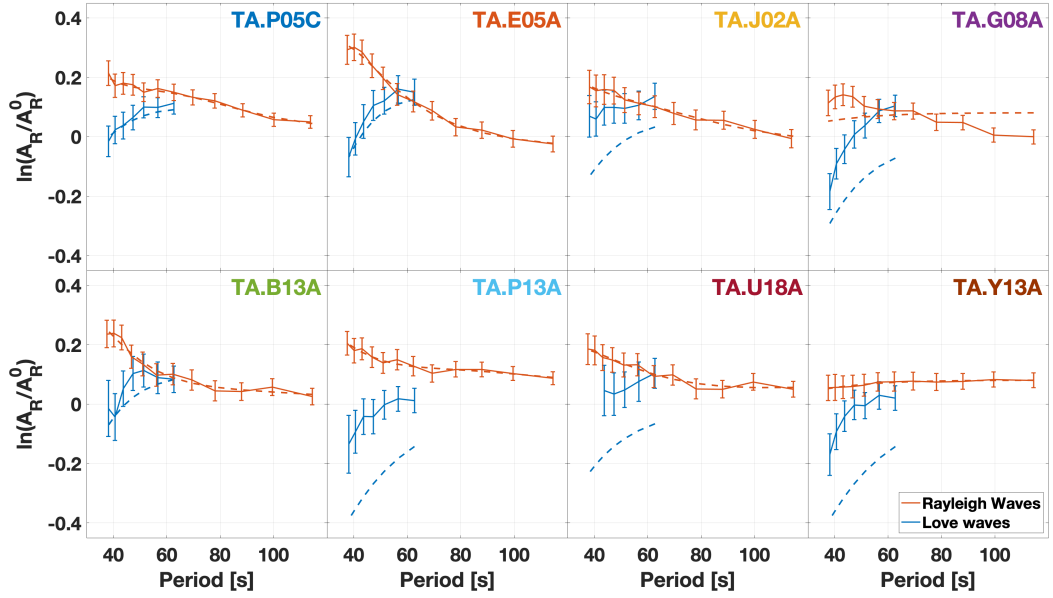


Figure 2. Comparisons of measured (solid lines with error bars) and theoretical amplification curves (dashed lines), calculated using 1-D profiles from SWUS-amp Schardong et al. (2019). Each illustrative station, given in the top-right of each panel, resides in a different major tectonic province (see Figure 1). Amplification curves for Rayleigh waves are shown in red, while for Love waves are shown in blue.

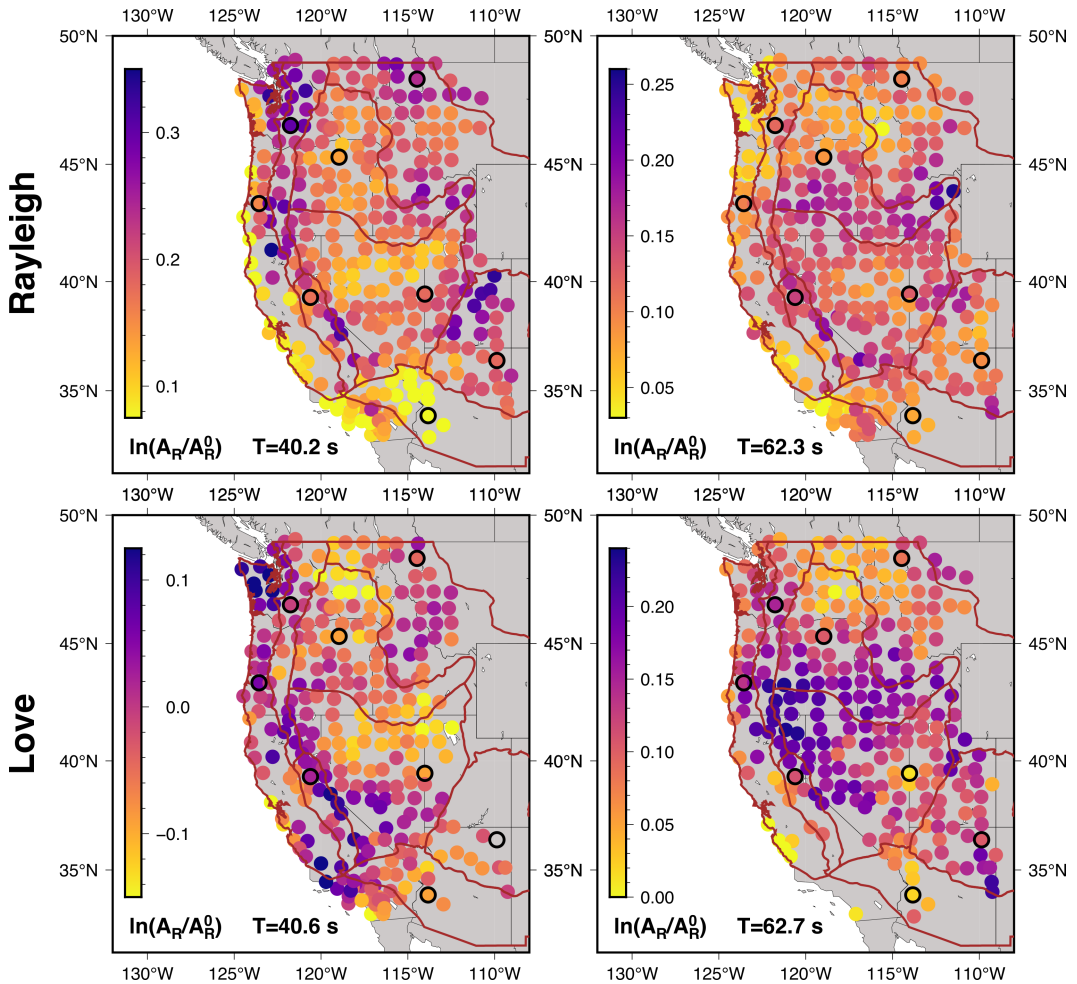


Figure 3. Top row: Rayleigh wave amplification measurements at $T \sim 40$ s (left) and $T \sim 62$ s (right). Bottom row: Love wave amplification measurements at $T \sim 41$ s (left) and $T \sim 63$ s (right). The eight illustrative stations shown in Figure 1 are highlighted with black borders. Brown lines outline the major tectonic provinces.

220 SWUS-amp (Schardong et al., 2019). Each station resides in a different major tectonic
 221 province (Figure 1), in order to show the range of amplification curves available in the
 222 western U.S. Given that SWUS-amp was built using the same Rayleigh wave dataset as
 223 in this study, the fit between the theoretical and observed Rayleigh wave amplification
 224 curves is excellent. However, the Love wave theoretical curves show a range of data fits.
 225 Whilst stations TA.P05C and TA.E05A show reasonable data fits, other stations show
 226 very poor fit, such as TA.U18A and TA.Y13A. Given the strong sensitivity of Love waves
 227 to the crust, as can be seen in Figure S2, this suggests that using Love wave amplification
 228 may help to constrain a more detailed crustal model than in SWUS-amp.

229 Figure 3 shows the local amplification measurements obtained for the available sta-
230 tions at wave periods of $T \sim 40$ s and $T \sim 62$ s. The Rayleigh and Love wave amplifica-
231 tion maps look different to one another because of their distinct sensitivities, however
232 there are also some common features. At $T \sim 40$ s for Rayleigh waves, low-local ampli-
233 fication is retrieved in the South Basin & Range and along the Pacific coastline. Con-
234 versely, high amplifying structures are retrieved along the Sierra Nevada and Cascade
235 ranges, and at the northeastern edge of the Colorado Plateau. At $T \sim 62$ s, high ampli-
236 fication is imaged along the southern Columbia Basin and Snake River Plain. This is in
237 contrast with the low-amplifying structures in the along the Pacific border, the North
238 Rocky Mountain and in the northernmost part of the Columbia Basin (see Figure 1 for
239 the geographical location of these regions).

240 At $T \sim 40$ s for Love waves, we observe low-amplifying structures beneath the Columbia
241 Basin and northeastern Basin & Range. Highly-amplifying structures are observed along
242 the northern Pacific coast and the western border of the North Basin & Range. At $T \sim 62$
243 s, there are highly-amplifying structures across the North Basin & Range, the Cascade
244 Range and the southern Columbia Basin. This is in contrast to the northern Columbia
245 Basin, Northern Rockies and southern Pacific border.

246 Previous studies have shown that local Rayleigh wave amplification shows a cor-
247 relation with crustal thickness (H. Gilbert, 2012; Eddy & Ekström, 2014). We observe
248 a similar pattern in Figure 3, where the thick crust beneath the Sierra Nevada Moun-
249 tains, Northern Rocky Mountains and Snake River Plain shows high-amplification, whereas
250 the thinner crust beneath the Columbia Basin, North and South Basin & Range and Pa-
251 cific coast shows low-amplification. Likewise, the Love wave amplification maps show a
252 similar correlation to crustal thickness.

253 The propagated amplification errors (Equation 6) can be seen for each station in
254 Figure 4, for the same illustrative wave periods. For both Rayleigh and Love wave am-
255 plification error maps, the errors are largest around the edges. The reason for this is be-
256 cause the number of stations pairs is lower for the outer stations (see Figure S3a), and
257 consequently the azimuthal coverage of station pairs is also lower (Figure S3b). Prop-
258 agated errors are greater for Love waves because in general horizontal component data
259 are noisier than vertical component data.

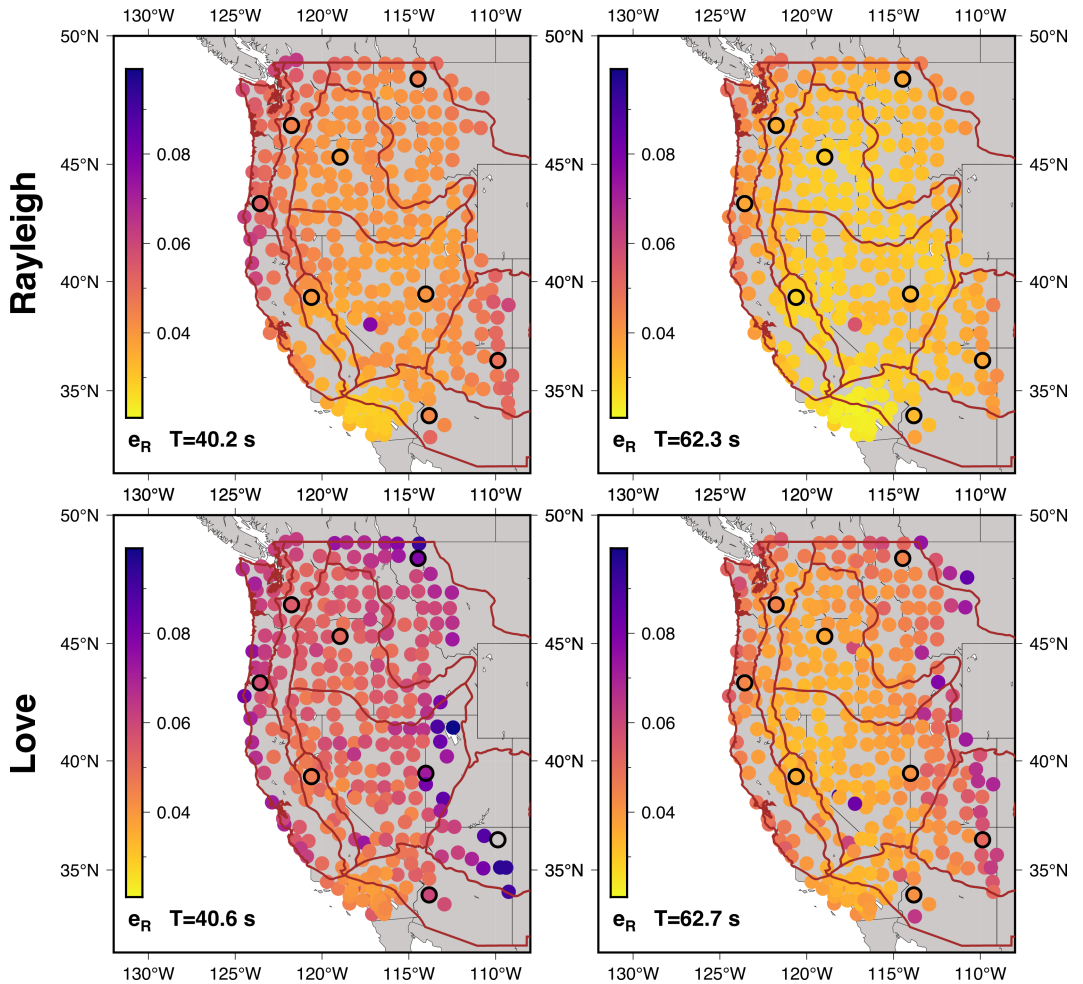


Figure 4. Top row: Rayleigh wave amplification error measurements at $T \sim 40$ s (left) and $T \sim 62$ s (right). Bottom row: Love wave amplification error measurements at $T \sim 41$ s (left) and $T \sim 63$ s (right). The eight illustrative stations are highlighted with black borders. The major tectonic provinces are outlined in solid brown lines.

260 **3 Inverting surface wave amplification for crustal shear wave speed**

261 **3.1 Inversion method**

262 There is a non-linear relation between surface-wave amplification and Earth struc-
 263 ture. We therefore use the fully non-linear Neighbourhood Algorithm (NA; Sambridge,
 264 1999) to jointly invert the observed amplification curves for depth-dependent v_S beneath
 265 each available station. The NA is a Monte Carlo based approach that divides the pa-
 266 rameter space into Voronoi cells (Voronoi, 1908) to quickly find an ensemble of models
 267 that best fit the data. The NA has been used to constrain crustal structure in a num-
 268 ber of different settings, including in the western U.S. (e.g., Moschetti et al., 2010a), Por-
 269 tugal (Attanayake et al., 2017), northern Italy (Berbellini et al., 2017), the Azores (Ferreira
 270 et al., 2020), central Java (Ariyanto et al., 2018), the Netherlands (Yudistira et al., 2017)
 271 and Greenland (Jones et al., 2021). The NA is composed of two main stages. Firstly, the
 272 NA randomly samples the parameter space and each model is ranked according to its
 273 misfit between the observed and theoretical amplification curves. Secondly, the NA en-
 274 ters an optimisation stage where in each iteration models are sampled within the neigh-
 275 bourhood of the best-fitting models. After extensive testing, in the initial stage we choose
 276 to sample 2,000 random models. Then, in the second stage, for each iteration the NA
 277 picks 20 models within the neighbourhood of the best five models from the previous it-
 278 eration. Moreover, the NA proceeds for 500 iterations to ensure the solution converges
 279 on the same model each time. Figure S4 shows an example of misfit evolution, clearly
 280 showing good convergence.

281 We use a L_2 -norm misfit function:

$$s(\mathbf{m}) = \sum_{i=1}^N \frac{(A_{R,i} - g_i(\mathbf{m}))^2}{e_{R,i}^2} \quad (7)$$

282 where $g_i(\mathbf{m})$ is the predicted amplification for the model \mathbf{m} being sampled, $A_{R,i}$
 283 is the observed amplification, $e_{R,i}$ is the observed error, N is the number of wave peri-
 284 ods and i is the individual wave period.

285 We ran a number of synthetic tests to verify if the addition of Love wave ampli-
 286 fication data helps to further constrain mantle v_S compared to using Rayleigh wave am-
 287 plification data alone, but extensive testing revealed that due to their strong sensitiv-
 288 ity to the crust, they could not constrain the mantle. Next, due to Love wave amplifi-
 289 cation being mainly sensitive to v_{SH} , we performed joint inversions of Rayleigh and Love

wave amplification data for a radially anisotropic crust, but the increased number of parameters that needed to be inverted for with a relatively small dataset led to unstable inversions. Hence, we invert for an isotropic crust, and have verified that the data fit is good for both Love and Rayleigh wave data (i.e., we ensured that the data used in this study do not require radial anisotropy). Given that crustal layers typically have strong contrasts in seismic properties and the success of previous studies in using layered parameterisations for the crust, notably with three layers (e.g., Laske et al., 2012; Schmandt et al., 2015; Ferreira et al., 2020), we decided to also use a three-layered crustal parameterisation. Since our mantle model SWUS-amp (Schardong et al., 2019) was successfully built using Moho depths from CRUST1.0, we also constrain the depths of our three-layer crustal model using CRUST1.0 (Figure S5). We choose not to invert for sediment layers, as that would require shorter period amplification measurements.

One of the advantages of using the NA is that it provides an ensemble of models that can be used to estimate uncertainties for our final solution. We calculate the perceptual uncertainty e_{v_s} for each station used to build our model by considering the range of velocities, $v_{s,\max} - v_{s,\min}$, of all models within a 20% misfit of the best-fitting model, $v_{s,\text{best}}$, in each crustal layer.

$$e_{v_s} = \frac{(v_{s,\max} - v_{s,\min})}{v_{s,\text{best}}} \times 100 \quad (8)$$

We choose a threshold of 20% because it includes models that fit the amplification curves reasonably well. A looser threshold would include models with a poor data fit, and a stricter threshold would not be representative of the range of models that fit the data relatively well.

We invert for v_S whilst scaling for v_P and ρ using the general Brocher relation (Brocher, 2005). The mantle structure is fixed to that of SWUS-amp (Schardong et al., 2019) between the Moho and ~ 300 km depth and to PREM beneath this depth. In the next section we will justify this choice of mantle model with the help of synthetic inversion tests and trade-off tests between crustal and mantle structure. Constraints are imposed on the inversion whereby v_S must increase with depth within each crustal layer as well as beneath the Moho. Previous crustal models in the western U.S. show that v_S always increases with depth within these ranges (e.g., Schmandt et al., 2015; Shen & Ritzwoller, 2016) and our inversion tests showed that these constraints help stabilise the inversions.

320 We invert for shear-wave velocity perturbations ($\frac{\delta v_S}{v_S}$), with respect to the average crustal
 321 v_S of PREM. In order to search a wide range of possible model parameters, we allow the
 322 inversion to search between $\pm 40\%$ of the average crustal v_S of PREM in each layer.

323 **3.2 Synthetic inversion tests**

324 We perform synthetic inversion tests to investigate how capable our inversion method
 325 is of retrieving realistic input crustal models. We use the results from our best real data
 326 inversion model as our input model, in order to perform the tests on realistic models.
 327 Gaussian random noise is added to each data point by simulating 200 predicted ampli-
 328 fication curves using the standard deviations of the real data measurements. The aver-
 329 age amplification curve and standard deviation of these simulated curves are used as the
 330 input synthetic data into the NA as described in section 3.1.

331 Figure 5 shows the results from synthetic inversions for our 8 stations of interest.
 332 Overall, the synthetic inversions work very well, showing that the NA converges to the
 333 input model even with noise introduced. Models within a 20% misfit of the best retrieved
 334 model are shown by coloured lines and it is encouraging to see that these models show
 335 a small range in velocities, centred around the best-fitting model. There are, however,
 336 some slightly imperfect solutions which are due to trade-offs in v_S between the crustal
 337 layers (e.g., for stations TA.P05C and TA.G08A).

338 In order to investigate model parameter trade-offs in our inversions further, we pro-
 339 duce trade-off plots by plotting all the crustal and mantle model parameters used in the
 340 inversions against each other (see e.g., Figure S6 for station TA.Y13A). Furthermore,
 341 we perform inversions inverting not only for the three crustal layers but also for the v_S
 342 coefficients of one spline function describing the uppermost mantle structure between the
 343 Moho and ~ 90 km depth. This ensures that we are not biasing our crustal model by fix-
 344 ing the mantle to SWUS-amp. Figure S7 in the supplementary information shows that
 345 there is a small trade-off in v_S between the uppermost mantle and lower crust, indicat-
 346 ing that fixing v_S in the mantle does not significantly affect the retrieved crustal model.
 347 This also highlights the fact that Love waves have low sensitivity to the uppermost man-
 348 tle, but add important sensitivity to the crust, as can be seen by the sharp gradient in
 349 sensitivity in Figure S2. Conversely, Rayleigh waves show strong sensitivity to the crust

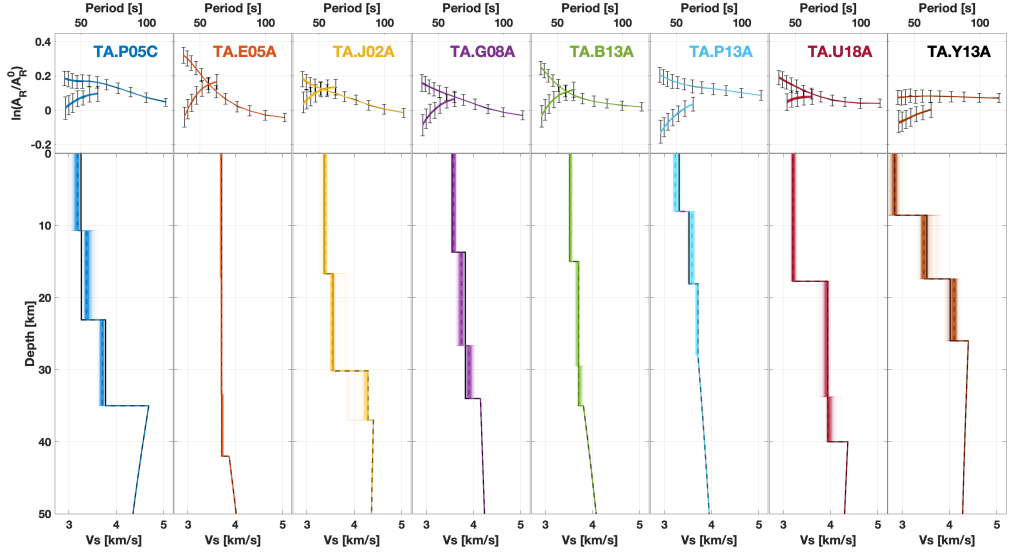


Figure 5. Example of results from synthetic inversion tests. Top row: amplification curves computed for synthetic input 1-D v_S profiles (black lines with error bars) and the retrieved output 1-D v_S profiles (coloured lines). The curves with longer periods are for Rayleigh waves, and the shorter curves are for Love waves. Bottom row: Corresponding input (black dashed lines) and output (bold coloured lines) v_S models. The more transparent coloured lines show the models with misfit values within 20% of the model with the lowest misfit.

and uppermost mantle, but, as found by Schardong et al. (2019), they cannot constrain alone crustal models more complex than a single layer.

3.3 Results from real data inversions

We jointly invert Rayleigh and Love wave amplification curves for 1-D v_S profiles using the NA as described in Section 3.1. Figure 6 shows examples of 1-D v_S profiles obtained for the eight illustrative stations located within each major tectonic province in the western U.S considered in this study. For reference, we compare our model with the layered crustal model of Schmandt et al. (2015) and the smooth crustal model of Shen and Ritzwoller (2016), which were built using completely independent data sets from this study. As with the synthetic profiles in Figure 5, we plot all models with a data misfit within 20% of the best-fitting model. These models are clustered around the best-fitting model, showing that we have a well-converged solution and that any trade-offs appar-

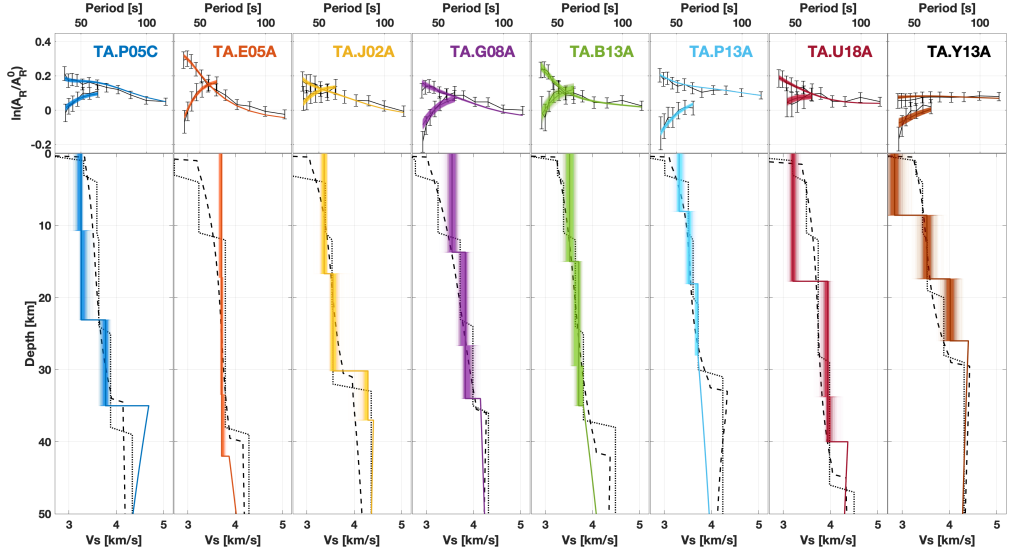


Figure 6. Real data inversions for depth-dependent v_S for the eight example stations located in each major tectonic province in the western U.S. (see Figure 1). Top row: Amplification curves for Rayleigh waves (long curves) and Love waves (short curves) for real data (black lines with error bars), the best retrieved model (thick coloured lines) and models within a 20% misfit value of the best-fitting model (thin coloured lines). Bottom row: 1-D shear-velocity crustal profiles for SWUS-crust (coloured lines), compared to the models of Schmandt et al. (2015) (dotted lines) and Shen and Ritzwoller (2016) (dashed lines).

362 ent in the model do not have a significant impact on our final model. Figure S4 shows
 363 an illustrative example of convergence of an inversion for station TA.P13A. It can be seen
 364 that convergence is achieved after 10,000 models but we continue the inversion up to 12,000
 365 models for insurance.

366 We compare SWUS-crust to the single crustal layer of SWUS-amp (Figure S1) to
 367 further check if our modelling is biased by the presence of anisotropy. Similar crustal fea-
 368 tures are seen in SWUS-amp compared to SWUS-crust, for example high v_S beneath the
 369 Columbia basin, Colorado Plateau and Northern Rocky mountains. Similarly, low v_S is
 370 observed beneath parts of the Northern Basin & Range and the High Lava Plains. Such
 371 similarities suggest that the inclusion of Love wave amplification data in SWUS-amp has
 372 not introduced a bias due, e.g., to radial anisotropy. Furthermore, as mentioned previ-
 373 ously, SWUS-amp does not fit Love wave data well, as seen in Figure 2. We ran several

374 anisotropic and isotropic inversions including Love waves and whilst isotropic inversions
 375 remained robust, anisotropic inversions were not. The data fit for both Rayleigh and Love
 376 waves is good, but is not always perfect, indicating that a small amount of anisotropy
 377 could be present, and indicating no clear bias. Future robust modelling of crustal anisotropy
 378 requires the inclusion of further data types such as, e.g., dispersion data.

379 There are similarities and differences between the various 1-D v_S profiles. We no-
 380 tice that our results obtained for the lower- and mid-crustal layer match the other mod-
 381 els well, but there are some differences in the upper-crustal layer. In some profiles we
 382 observe higher upper-crustal v_S values (e.g., for stations TA.E05A, TA.G08A) and in
 383 other cases we observe lower upper-crustal v_S (e.g., TA.U18A, TA.Y13A). The geograph-
 384 ical differences in the velocities and the model uncertainties will be discussed in detail
 385 in the next section.

386 The 1-D v_S profiles are interpolated laterally for each layer using an ordinary krig-
 387 ing routine to obtain a new 3-D crustal model in the western U.S. This technique was
 388 successfully used in previous imaging studies (e.g., Berbellini et al., 2017; Schardong et
 389 al., 2019; Jones et al., 2021), as the technique allows for interpolation of sparse or irreg-
 390 ularly sampled data.

391 In order to estimate the spatial covariance amongst our stations, we first constructed
 392 a semi-variogram. This quantifies the degree of variability in the inferred velocities as
 393 a function of the separation distance. A “spherical model” is used to quantify the increase
 394 in variability with increased separation distance. The extracted parameters from the semi-
 395 variogram describing how the velocities at stations covary with separation distance are
 396 used to model the covariance between velocities at stations and velocities across a uni-
 397 form grid.

398 We explore a range of models to fit the semi-variogram (for example in the upper
 399 crustal layer, Figure S8), and choose a spherical model as it both fits the semi-variogram
 400 well and shows relatively low interpolation uncertainty. We note that, as expected, un-
 401 certainties in the interpolated values decrease in areas with high station coverage. Fig-
 402 ure 7 shows the model before and after interpolating the profiles. We refer to the result-
 403 ing model as SWUS-crust, whose key features will be discussed in the next section. For
 404 completeness, we also show SWUS-amp in terms of absolute v_S in Figure S9.

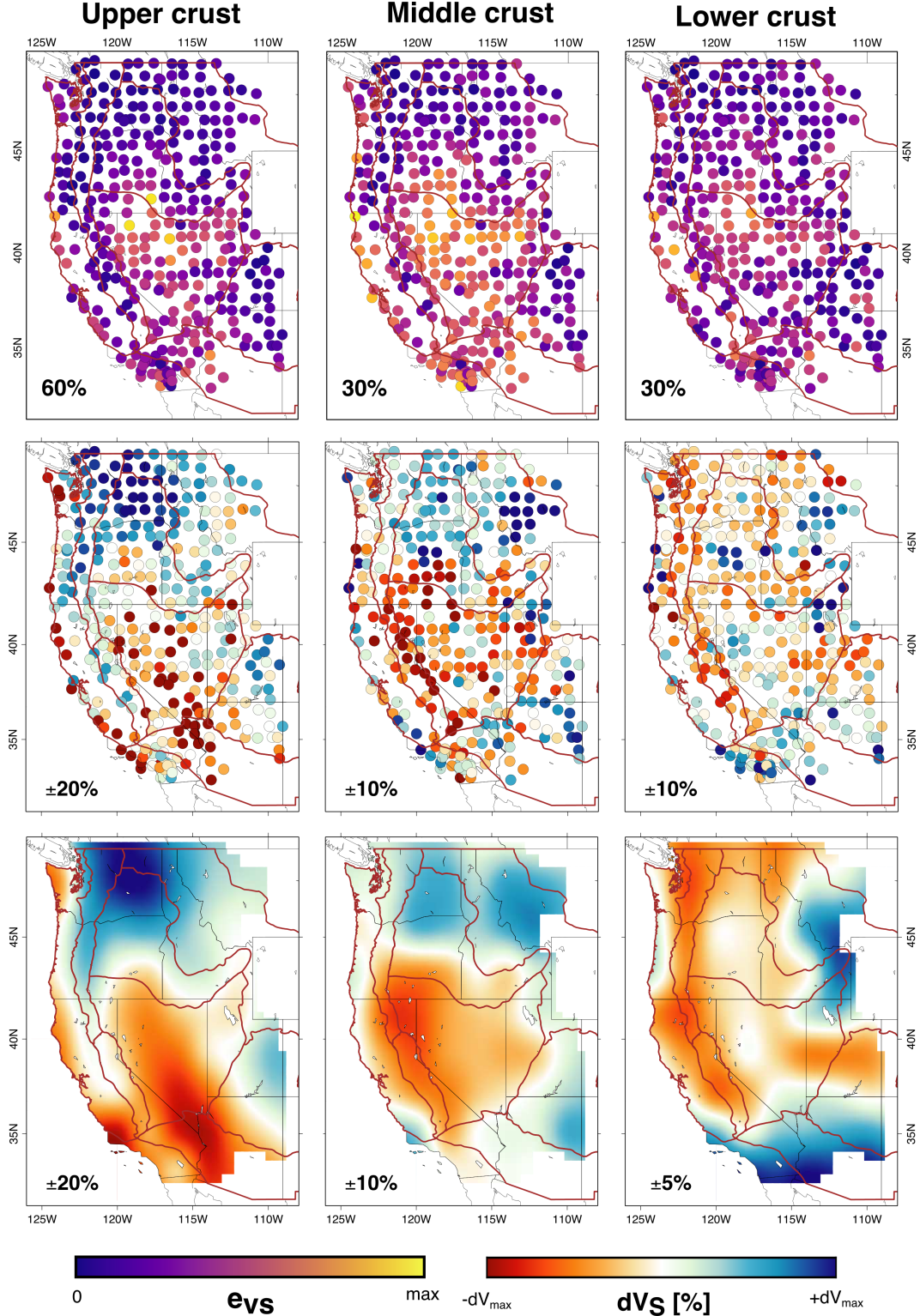


Figure 7. Top row: Maps of percentual model uncertainties, as defined by Equation 8, for each station used in the construction of SWUS-crust. The maximum of the scale bar is indicated in the bottom left of each panel. Middle row: Deviations from the average vs in each layer, in the upper, middle and lower crust at each station for our model SWUS-crust. Bottom row: the same as the top row but after kriging interpolation (see text for further details).

405 Figure 7 also shows the uncertainty of our real data inversions in each crustal layer,
 406 as defined by Equation 8. There appears to be a relation between crustal thickness and
 407 model uncertainty, whereby the regions of thinnest crust (e.g., North and South Basin
 408 & Range, Pacific Coast) have the highest uncertainty. The crustal thickness in CRUST1.0,
 409 in general, is shallower than in Shen and Ritzwoller (2016), who used receiver functions
 410 to help constrain the Moho depth, as can be seen in Figures 5 and 6. As a result, we re-
 411 ran our inversions changing the Moho depth to that defined by Shen and Ritzwoller (2016)
 412 for four stations in the North Basin & Range, as seen in Figure S6. Uncertainty in the
 413 lower crust decreased by $\sim 3\%$, which is not very substantial. This suggests that uncer-
 414 tainties in Moho depth defined by CRUST1.0 do not significantly affect the uncertainty
 415 in our model. Model uncertainties in the upper crust are generally higher compared to
 416 the middle and lower crust. This is likely due to the fact that we do not invert very short
 417 period data, which would be most sensitive to upper crustal depths.

418 4 Discussion

419 Previous studies of the crustal structure of the western U.S. have used various com-
 420 binations of data, including surface wave dispersion data from both seismic ambient noise
 421 and teleseismic events, Rayleigh wave ellipticity measurements and receiver functions.
 422 In this study we built the first crustal model based on Rayleigh and Love amplification
 423 data alone with wave periods $T > 38$ s. As shown by the synthetic tests presented in sec-
 424 tion 3.2, the narrow depth sensitivity of these observables (Figure S2) enables the con-
 425 struction of our new detailed crustal model of the western U.S., SWUS-crust.

426 4.1 Comparison with other models

427 Table S1 in the Supporting Information provides details on the data sets, param-
 428 eterisation, forward modelling, inversion methods and constraints used by other mod-
 429 els discussed in this study; Laske et al. (2012); Moschetti et al. (2010a); Schmandt et al.
 430 (2015); Shen and Ritzwoller (2016); Porter et al. (2016); Xie et al. (2018); Chai et al. (2015).

431 Figure 8 compares SWUS-crust with other crustal layered models of the western
 432 U.S., including the global crustal model CRUST1.0 (Laske et al., 2012), the regional mod-
 433 els of Moschetti et al. (2010a) and Schmandt et al. (2015). Whilst we do not invert for
 434 sedimentary layers, we choose to show them for the other models to aid our interpreta-

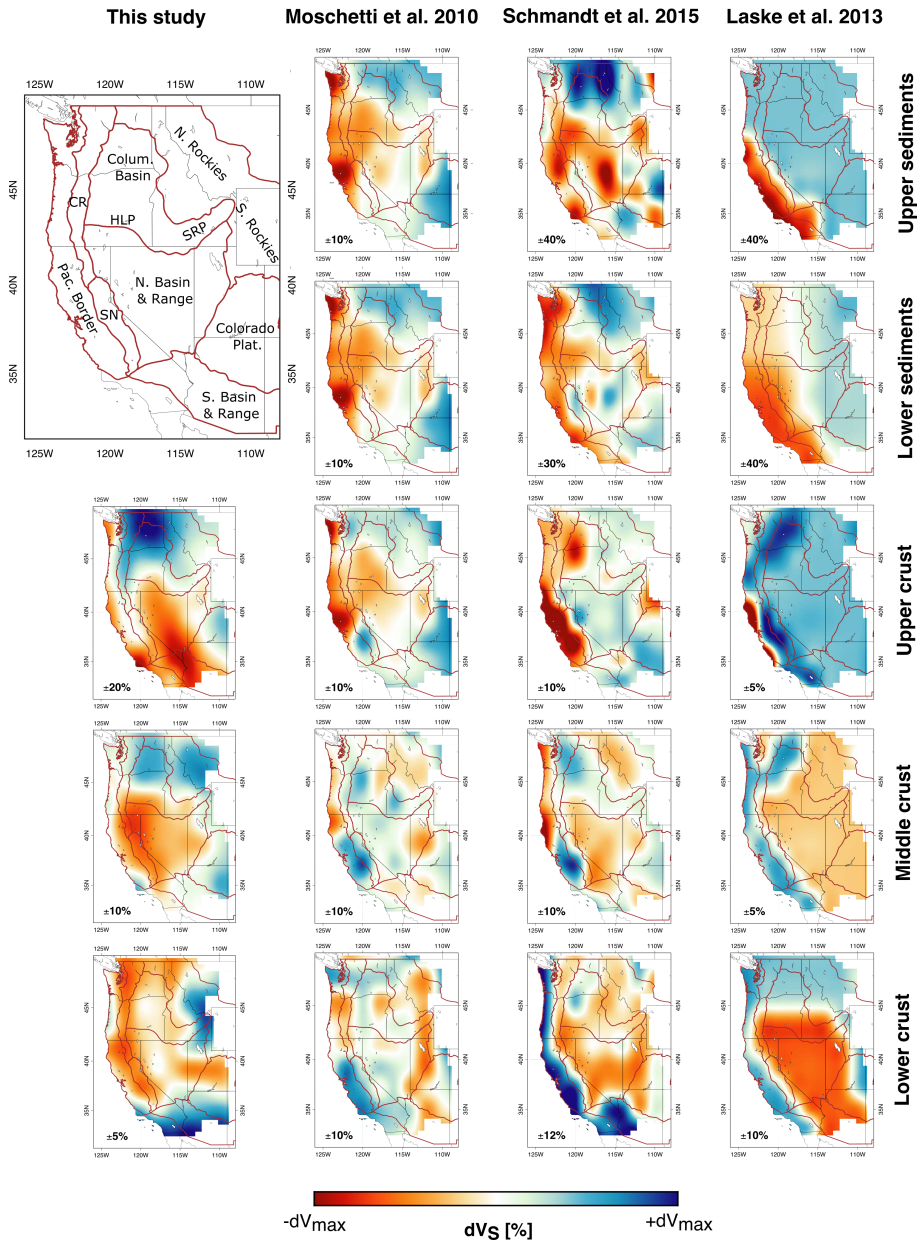


Figure 8. Comparison of the SWUS-crust v_S model (first column) with other layered crustal models, the model of Moschetti et al. (2010a), US-CrustVs-2015 (Schmandt et al., 2015) and CRUST1.0 (Laske et al., 2012). SWUS-crust does not constrain sedimentary layers, hence there are missing panels. In their place is a map showing the location of key tectonic features that are discussed. For each map, the velocity perturbations are presented with respect to the average velocity of that map. The limits of the perturbations are given in the bottom-left of each map and the boundaries of each tectonic province are shown by brown lines.

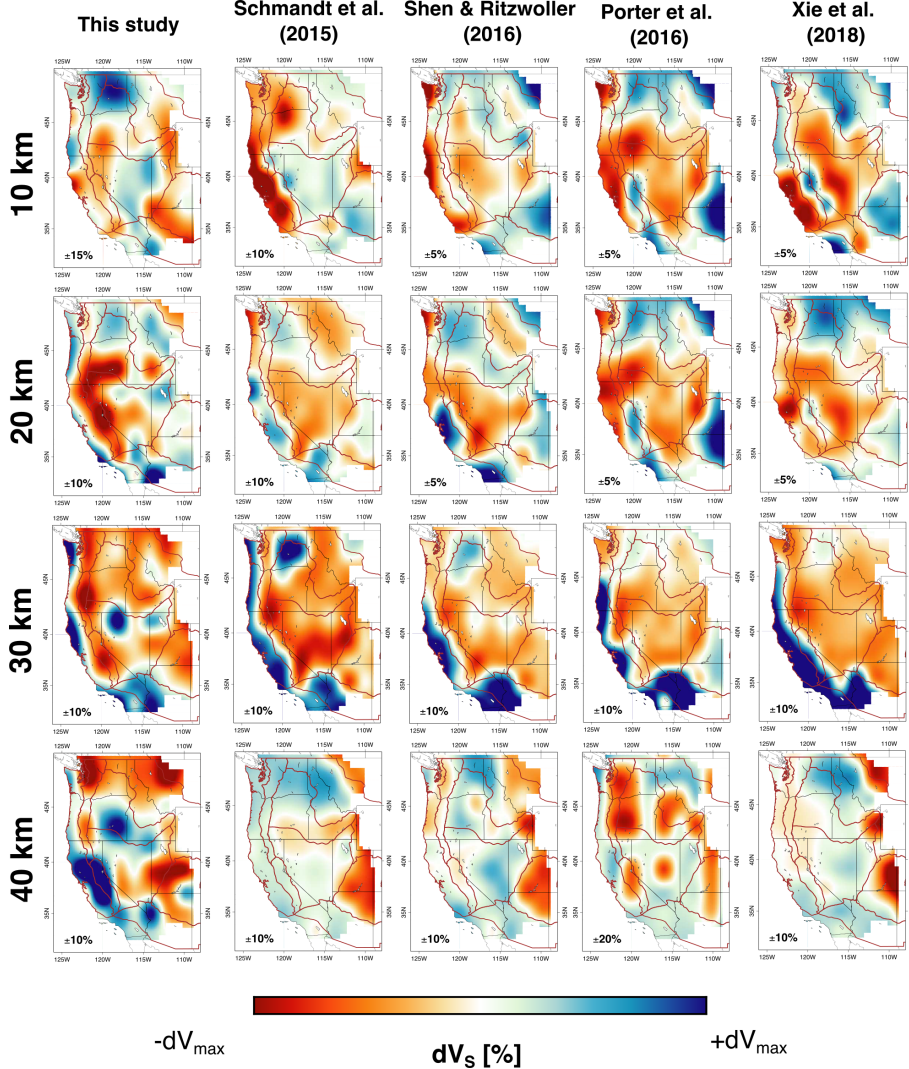


Figure 9. Comparison of the SWUS-crust (first column) with other local tomographic models; Schmandt et al. (2015); Shen and Ritzwoller (2016), Porter et al. (2016) and Xie et al. (2018) at depths of 10, 20, 30 and 40 km. The velocity perturbations of all models are expressed with respect to the average velocity at each depth respectively. The bounds of the colour scale are shown in the bottom-left of each map and the boundaries of each tectonic province are shown by brown lines. The lateral borders of SWUS-crust is also added to each model in order to aid in their comparisons.

435 since the upper crust layer of SWUS-crust may also reflect shallower sedimentary
 436 structures. In addition to these models, we also compare SWUS-crust to a number of
 437 smoothly parameterised crustal models at depth intervals of 10 km, (Figure 9) Shen and
 438 Ritzwoller (2016); Porter et al. (2016); Xie et al. (2018) and intervals of 5 km for fur-
 439 ther models in Figure S10 (Chai et al., 2015).

440 Figures 7 and 8 show that there are some similarities between the different mod-
 441 els, notably between the models with a layered parameterisation shown in Figure 8, which
 442 show for example mostly low crustal v_S anomalies along the Pacific coast in the upper
 443 crust and high crustal v_S anomalies beneath the Columbia basin in the middle crust. On
 444 the other hand, there are also considerable differences between the models, notably re-
 445 garding their small scale structures. For example, SWUS-crust shows a lot of regional
 446 variations compared to CRUST1.0 (Figure 8) and the model of Chai et al. (2015) (Fig-
 447 ure S10), while other models show more comparable small-scale heterogeneity.

448 4.2 The Northern Rockies, the Columbia basin and High Lava Plains

449 Figures 7 and 8 show that SWUS-crust images a high v_S anomaly in the upper and
 450 middle crust beneath the Northern Rocky mountains, but a slower anomaly in the lower
 451 crust. Specifically, at 10 and 15 km depths in Figure S10, the Northern Rockies are un-
 452 derlain by low v_S anomalies, largely matching other models at these depths (e.g., Schmandt
 453 et al., 2015; Laske et al., 2013; Chai et al., 2015). This could be explained by intense mag-
 454 matism during the Cenozoic, prior to uplift in the region (Tesauro et al., 2014). There
 455 is little consistency between models in the middle and lower crust beneath this region
 456 (Figure 8; see also the differences e.g., at depth slices of 20 and 35 km in Figure S10).

457 Figure 8 shows that the signature of the Columbia basin in SWUS-crust is a high
 458 v_S anomaly throughout the upper and middle crust, with its magnitude decreasing strongly
 459 with depth. A similar trend is observed in all models, with the exception of Schmandt
 460 et al. (2015) and Moschetti et al. (2010a) which show low v_S anomalies in the upper crust.
 461 This anomaly could be related to a mafic composition following continental rifting dur-
 462 ing the initiation of the Cascadia subduction zone (Catchings & Mooney, 1988b; Schmandt
 463 & Humphreys, 2011). It is worth noting that, as explained previously, we do not invert
 464 for sediment layers as they are too thin to be constrained by our data, which have a min-
 465 imum period of 38 s. Therefore care must be taken when comparing our model with oth-

ers at shallow depths (e.g., 5-10 km), the depths at which other models image sediments, while our images may show a mix of sediments and other deeper structures (Figure 9 and S10). For example, the Columbia basin is covered by a thick layer of Miocene flood basalts (Catchings & Mooney, 1988b, 1988a) which we might have imaged in the upper crustal layer. This anomaly is similarly reflected in the upper sediments of Schmandt et al. (2015).

In order to further explore the differences observed beneath the Columbia basin between our model and the model of Schmandt et al. (2015), we computed theoretical amplification curves for the input model of Schmandt et al. (2015) at the points of the model nearest to nine illustrative stations shown in Figure S11. The same test was performed using the model made by Shen and Ritzwoller (2016), as shown in Figure S12. These two models show the Columbia basin, in particular the Yakima Fold Belt in the western part of the basin, as largely a low-velocity anomaly in the upper crust. Therefore we ran a test to see if these models fit our observations. Forward modelling of these models shows that neither fits all data particularly well (Figures S11, S12). The model of Shen and Ritzwoller (2016) fits the Love wave amplification curves well, but not the Rayleigh wave curves at short periods ($T \sim 35\text{-}70$ s). In contrast, the model of Schmandt et al. (2015) fits the Rayleigh wave data rather well, but not the Love wave data. This test helps us to confirm that the surface wave amplification data require the observed fast v_S anomaly and that this anomaly is not due e.g., to the model parameterisation chosen. Both models use similar data types, so the observed differences could be due to their choice of inversion scheme.

The High Lava Plains (HLP in Figure 8), located in central Oregon, form a boundary between the Basin & Range province to the south and the Columbia basin to the north. This is also represented in Figure 8, where the HLP divide the high v_S anomalies of the Columbia basin with the low v_S anomalies of the North Basin & Range. In all layers of SWUS-crust, low v_S anomalies are observed beneath the HLP and the northern border is particularly well delineated in the middle crustal layer. The plains are also well delineated in CRUST1.0 but not in its upper crustal layer, while Moschetti et al. (2010a) only observed this low v_S anomaly in the upper crust. The anomaly observed in SWUS-crust throughout the entire crust may be explained by a magma injection due to recent volcanism along the Yellowstone hotspot track (Jordan et al., 2004).

497 **4.3 The Pacific coast, the Cascade range and Snake River Plain**

498 SWUS-crust shows low v_S anomalies in the upper crust beneath the Pacific coast
 499 (Figure 8), similarly to other models, and high v_S anomalies between 20-40 km depth
 500 (Figure 9 and Figure S10), which may reflect mafic material formed by accreted oceanic
 501 crust (Lin et al., 2014). SWUS-crust does not show a clear anomaly beneath the Great
 502 Valley in California, unlike the clear observation in the middle crust in the models of Moschetti
 503 et al. (2010a) and Schmandt et al. (2015). However, when studying the station distri-
 504 bution in Figure 7, there is a clear lack of stations considered in the valley.

505 In the Cascade range, we observe high v_S anomalies in the upper crust underlain
 506 by a neutral v_S anomaly in the middle crust and a low v_S anomaly in the lower crust.
 507 No clear trend is observed beneath the Cascade range in Figure 8, but it remains a con-
 508 sistently low v_S anomaly at 30 km depth in Figure 9, and at 35 km depth in Figure S10,
 509 with the exception of Laske et al. (2012). Low velocities at lower crustal depths may re-
 510 flect crustal thickening and/or warm mantle temperatures (Chai et al., 2015).

511 To the east, the Snake River Plain (SRP) is not associated with a continuous ve-
 512 locity anomaly region in our model, but instead shows several distinct anomalous fea-
 513 tures. In the upper crust the region shows high to low v_S anomalies from west to east,
 514 but the opposite is observed in the middle and lower crust. This could be related to more
 515 recent volcanism towards Yellowstone and to the intrusion of mafic material (Sparlin et
 516 al., 1982). In contrast, the models of Moschetti et al. (2010a) and Schmandt et al. (2015)
 517 do not show any clear crustal velocity anomalies along the SRP, with the exception of
 518 the lower crust, where there is a slow v_S anomaly at the end of the hotspot track towards
 519 Yellowstone. However, when looking at the depth slices in Figure 9, the majority of mod-
 520 els show low, or neutral v_S anomalies at 20-30 km depth. Stronger low v_S anomalies fur-
 521 thest east of the SRP at 30-40km in Figure 9 may be due to a partially melted, hot body
 522 of granitic composition (Smith et al., 1982).

523 **4.4 The North Basin and Range, the Sierra Nevada and the Colorado
 524 Plateau**

525 The North Basin and Range appears largely as a low v_S anomaly throughout SWUS-
 526 crust (Figures 7 and 8). Most models show a similar feature, although at 10 km depth
 527 in Figure 9, large portions of the North Basin and Range show high v_S anomalies, in agree-

528 ment with the model of Schmandt et al. (2015). Low v_S anomalies are consistent across
 529 all models in Figure 8 in the middle crust and between 20-30 km depth in Figure 9. This
 530 is with the exception of the thinnest parts of the North Basin and Range (see Figure S5)
 531 at the northern border. Low v_S anomalies in the middle crust may be related to exten-
 532 sional deformation, as Moschetti et al. (2010b) imaged strong crustal anisotropy in this
 533 region. In the lower crust, low v_S anomalies may reflect Quaternary volcanism (Walker
 534 et al., 2004) and more recent intrusion of melts into the lower crust (Lin et al., 2014),
 535 which may produce an area of high heat flow (Tesauro et al., 2014).

536 The nearby Sierra Nevada mountain range does not seem to be associated with clear,
 537 well defined anomalies in SWUS-crust, but shows a neutral v_S anomaly in the upper crust,
 538 which changes to a low v_S anomaly in the middle and lower crust. A few models, such
 539 as that of Moschetti et al. (2010a), Schmandt et al. (2015) and Laske et al. (2012) show
 540 the Sierra Nevada as a more neutral feature, especially in the mid and lower crustal lay-
 541 ers. In these models, the Sierra Nevada dissects the high v_S anomalies of the Pacific coast
 542 and Great Valley to the west, and the low v_S anomalies of the North Basin & Range to
 543 the east (see Figures 8 and 9).

544 Finally, the Colorado Plateau shows a largely high v_S anomaly in the upper and
 545 middle crust, generally agreeing with most other models in Figure 8, with the notable
 546 exception being the middle crust in CRUST1.0 (Laske et al., 2012). The fast v_S anom-
 547 lies observed in this region may be attributed to the mafic composition of the plateau
 548 as discussed, e.g., by Zandt et al. (1995). In addition, higher v_S anomalies in the cen-
 549 tre of the plateau compared to the boundaries in the upper crust may be related to cold
 550 temperatures, which is consistent with low heat flow measurements in the region (Blackwell
 551 & Richards, 2004). Figures 9 and S10 show that at lower crustal depths (>25 km) the
 552 plateau is largely associated with a low v_S anomaly, matching almost all other models.
 553 As discussed by Moschetti et al. (2010a), it remains unclear if this is due to thermal or
 554 compositional effects.

555 4.5 Limitations and future work

556 While this work showed that crustal structure can be constrained by surface wave
 557 amplification data alone, the use of shorter period data is needed to image smaller-scale
 558 structures. For example, in order to invert for thin sedimentary layers, we could include

559 ambient noise and ellipticity measurements to add sensitivity to the top few kilometers
 560 of the crust. Moreover, future joint inversions of amplification data along with surface
 561 wave dispersion measurements and receiver functions would help to further constrain v_S
 562 in the crust, and also the depths of the crustal layers. This may also help to improve the
 563 data fit, particularly for seismic stations in the North Basin and Range, as the layer depths
 564 will no longer have to be fixed to CRUST1.0. Finally, while thanks to a careful data se-
 565 lection we could fit both Rayleigh and Love wave amplification data well, by incorpo-
 566 rating further data types (dispersion, etc), in the future we may be able to constrain anisotropy
 567 in the mantle and crust. In turn, this could help significantly to interpret the model in
 568 terms of the tectonic and geodynamical evolution of the region.

569 5 Conclusions

570 We presented SWUS-crust, a crustal model of the western U.S. built with Rayleigh
 571 ($T \sim 38\text{--}115$ s) and Love ($T \sim 38\text{--}63$ s) wave amplification measurements. This is, to the
 572 best of our knowledge, the first time Love wave amplification measurements have been
 573 used to construct a seismic model. Love wave amplification measurements show a strong
 574 sensitivity to the crust and, when jointly inverted with Rayleigh wave amplification data
 575 using the Neighbourhood Algorithm, lead to a crustal model that is more detailed than
 576 its predecessor model, SWUS-amp (Schardong et al., 2019).

577 Due to its complex tectonic history, significant variability in shear-wave velocity
 578 is imaged across the western U.S. SWUS-crust clearly shows the fast Columbia basin in
 579 the upper and middle crust. Moreover, it shows distinct changes in velocity beneath the
 580 Colorado Plateau from generally high anomalies in the upper and mid crust, to lower
 581 anomalies in the lower crust, particularly at 30 km depth. We largely image the slow North
 582 Basin & Range throughout the whole crust. The High Lava Plains of central and south-
 583 eastern Oregon are imaged in finer detail compared to previous models. In particular,
 584 the northern border of the HLP in southern Oregon appears very well delineated in the
 585 middle layer of SWUS-crust.

586 6 Open Research

587 The surface wave amplification dataset used in this study is attributed to Schardong
 588 et al. (2022). The Neighbourhood Algorithm (Sambridge, 1999) can be downloaded from
 589 <http://iearth.edu.au/codes/NA/>. The normal mode package used in this study is Mi-

590 neos 1.0.2 (Masters et al., 2011) published under the GPL2 license. We thank the Com-
 591 putational Infrastructure for Geodynamics (<http://geodynamics.org>) which is funded
 592 by the National Science Foundation under awards EAR-0949446 and EAR-1550901. The
 593 other tomography models used in this study were obtained from the IRIS Earth Model
 594 Collaboration (<http://ds.iris.edu/ds/products/emc-earthmodels/>). ETOPO1 was
 595 downloaded from <https://www.ngdc.noaa.gov/mgg/global/>. All maps were built us-
 596 ing using Generic Mapping Tools software (Wessel & Smith, 1998).

597 Acknowledgments

598 We thank Matthew Fox for fruitful discussion and for his insight into the kriging anal-
 599 ysis. We also thank Eric Debayle and David Dobson for fruitful discussion. WS was sup-
 600 ported by NERC grant number NE/L002485/1. We gratefully acknowledge the avail-
 601 ability of global seismograms from the IRIS Data Services and the IU, II, GEOFON and
 602 GEOSCOPE networks. The seismic data analyses and inversions were carried out on the
 603 High Performance Computing Clusters Grace and Kathleen, supported by the Research
 604 and Computing Support services at UCL. We thank Hendrik van Heijst for providing
 605 his surface wave amplitude measurements.

606 References

- 607 Ariyanto, P., Rosid, S., Anggono, T., Januarti, Y., et al. (2018). Crustal structure
 608 in the southern part of central java based on analysis of tele-seismic receiver
 609 function using a neighbourhood algorithm. In *Journal of physics: Conference
 610 series* (Vol. 985, p. 012018).
- 611 Attanayake, J., Ferreira, A. M., Berbellini, A., & Morelli, A. (2017). Crustal struc-
 612 ture beneath portugal from teleseismic rayleigh wave ellipticity. *Tectono-*
 613 *physics*, 712, 344–361.
- 614 Bao, X., Dalton, C. A., & Ritsema, J. (2016). Effects of elastic focusing on global
 615 models of rayleigh wave attenuation. *Geophysical Supplements to the Monthly
 616 Notices of the Royal Astronomical Society*, 207(2), 1062–1079.
- 617 Bassin, C. (2000). The current limits of resolution for surface wave tomography in
 618 north america. *EOS Trans. AGU*. 81: Fall Meet. Suppl., Abstract.
- 619 Bateman, P. C., & Eaton, J. P. (1967). Sierra nevada batholith: The batholith was
 620 generated within a synclinorium. *Science*, 158(3807), 1407–1417.

- 621 Bensen, G., Ritzwoller, M., & Yang, Y. (2009). A 3-d shear velocity model of the
622 crust and uppermost mantle beneath the united states from ambient seismic
623 noise. *Geophysical Journal International*, 177(3), 1177–1196.
- 624 Berbellini, A., Morelli, A., & Ferreira, A. M. (2017). Crustal structure of northern
625 italy from the ellipticity of rayleigh waves. *Physics of the Earth and Planetary
626 Interiors*, 265, 1–14.
- 627 Blackwell, D., & Richards, M. (2004). Geothermal map of north america. american
628 association of petroleum geologist (aapg), 1 sheet, scale 1: 6,500,000. *Search
629 in.*
- 630 Braile, L., Hinze, W., Von Frese, R., & Keller, G. R. (1989). Seismic properties of
631 the crust and uppermost mantle of the conterminous united states and adja-
632 cent canada. *Geological Society of America Memoirs*, 172, 655–680.
- 633 Brocher, T. M. (2005). Empirical relations between elastic wavespeeds and density
634 in the earth's crust. *Bulletin of the seismological Society of America*, 95(6),
635 2081–2092.
- 636 Buehler, J., & Shearer, P. (2012). Localized imaging of the uppermost mantle with
637 usarray pn data. *Journal of Geophysical Research: Solid Earth*, 117(B9).
- 638 Catchings, R., & Mooney, W. (1988b). Crustal structure of the columbia plateau:
639 Evidence for continental rifting. *Journal of Geophysical Research: Solid Earth*,
640 93(B1), 459–474.
- 641 Catchings, R., & Mooney, W. D. (1988a). Crustal structure of east central oregon:
642 Relation between newberry volcano and regional crustal structure. *Journal of
643 Geophysical Research: Solid Earth*, 93(B9), 10081–10094.
- 644 Chai, C., Ammon, C. J., Maceira, M., & Herrmann, R. B. (2015). Inverting interpo-
645 lated receiver functions with surface wave dispersion and gravity: Application
646 to the western us and adjacent canada and mexico. *Geophysical Research
647 Letters*, 42(11), 4359–4366.
- 648 Chang, S.-J., Ferreira, A. M., Ritsema, J., van Heijst, H. J., & Woodhouse, J. H.
649 (2015). Joint inversion for global isotropic and radially anisotropic mantle
650 structure including crustal thickness perturbations. *Journal of Geophysical
651 Research: Solid Earth*, 120(6), 4278–4300.
- 652 Christensen, N. I., & Mooney, W. D. (1995). Seismic velocity structure and com-
653 position of the continental crust: A global view. *Journal of Geophysical Research:*

- 654 *Solid Earth*, 100(B6), 9761–9788.
- 655 Christiansen, R. L., Foulger, G., & Evans, J. R. (2002). Upper-mantle origin of
656 the yellowstone hotspot. *Geological Society of America Bulletin*, 114(10),
657 1245–1256.
- 658 Dalton, C. A., Bao, X., & Ma, Z. (2017). The thermal structure of cratonic litho-
659 sphere from global rayleigh wave attenuation. *Earth and Planetary Science
660 Letters*, 457, 250–262.
- 661 Dziewonski, A. M., & Anderson, D. L. (1981). Preliminary reference earth model.
662 *Physics of the earth and planetary interiors*, 25(4), 297–356.
- 663 Eddy, C. L., & Ekström, G. (2014). Local amplification of rayleigh waves in the
664 continental united states observed on the usarray. *Earth and Planetary Science
665 Letters*, 402, 50–57.
- 666 Ferreira, A. M., Marignier, A., Attanayake, J., Frietsch, M., & Berbellini, A. (2020).
667 Crustal structure of the azores archipelago from rayleigh wave ellipticity data.
668 *Geophysical Journal International*, 221(2), 1232–1247.
- 669 Ferreira, A. M., & Woodhouse, J. H. (2007). Observations of long period rayleigh
670 wave ellipticity. *Geophysical Journal International*, 169(1), 161–169.
- 671 Ferreira, A. M., Woodhouse, J. H., Visser, K., & Trampert, J. (2010). On the ro-
672 bustness of global radially anisotropic surface wave tomography. *Journal of
673 Geophysical Research: Solid Earth*, 115(B4).
- 674 Frietsch, M., Ferreira, A. M., & Funning, G. J. (2021). Data-driven two-fault mod-
675 eling of the mw 6.0 2008 wells, nevada earthquake suggests a listric fault rup-
676 ture. *Journal of Geophysical Research: Solid Earth*, 126(4), e2020JB020263.
- 677 Gilbert, F. (1971). Excitation of the normal modes of the earth by earthquake
678 sources. *Geophysical Journal International*, 22(2), 223–226.
- 679 Gilbert, H. (2012). Crustal structure and signatures of recent tectonism as influ-
680 enced by ancient terranes in the western united states. *Geosphere*, 8(1), 141–
681 157.
- 682 Hildreth, W. (2007). *Quaternary magmatism in the cascades: Geologic perspectives*.
683 US Geological Survey.
- 684 Huber, N. K. (1981). Amount and timing of late cenozoic uplift and tilt of the cen-
685 tral sierra nevada, california; evidence from the upper san joaquin river basin.
- 686 Humphreys, E. D., & Coblenz, D. D. (2007). North american dynamics and western

- 687 us tectonics. *Reviews of Geophysics*, 45(3).
- 688 Jones, G. A., Ferreira, A. M., Kulessa, B., Schimmel, M., Berbellini, A., & Morelli,
689 A. (2021). Uppermost crustal structure regulates the flow of the greenland ice
690 sheet. *Nature communications*, 12(1), 1–12.
- 691 Jordan, B. T., Grunder, A. L., Duncan, R. A., & Deino, A. L. (2004). Geochronol-
692 ogy of age-progressive volcanism of the oregon high lava plains: Implications
693 for the plume interpretation of yellowstone. *Journal of Geophysical Research:*
694 *Solid Earth*, 109(B10).
- 695 Laske, G., Masters, G., Ma, Z., & Pasyanos, M. (2012). Crust1. 0: An updated
696 global model of earth’s crust. *Geophys Res Abs*, 14, 3743.
- 697 Laske, G., Masters, G., Ma, Z., & Pasyanos, M. (2013). Update on crust1. 0—a 1-
698 degree global model of earth’s crust. In *Geophys. res. abstr* (Vol. 15, p. 2658).
- 699 Lin, F.-C., Moschetti, M. P., & Ritzwoller, M. H. (2008). Surface wave tomogra-
700 phy of the western united states from ambient seismic noise: Rayleigh and
701 love wave phase velocity maps. *Geophysical Journal International*, 173(1),
702 281–298.
- 703 Lin, F.-C., Tsai, V. C., & Ritzwoller, M. H. (2012). The local amplification of
704 surface waves: A new observable to constrain elastic velocities, density, and
705 anelastic attenuation. *Journal of Geophysical Research: Solid Earth*, 117(B6).
- 706 Lin, F.-C., Tsai, V. C., & Schmandt, B. (2014). 3-d crustal structure of the west-
707 ern united states: application of rayleigh-wave ellipticity extracted from noise
708 cross-correlations. *Geophysical Journal International*, 198(2), 656–670.
- 709 Masters, G., Woodhouse, J., & Freeman, G. (2011). Mineos v1. 0.2 [software]. *Com-*
710 *putational Infrastructure for Geodynamics*.
- 711 Moschetti, M., Ritzwoller, M., Lin, F., & Yang, Y. (2010b). Seismic evidence for
712 widespread western-us deep-crustal deformation caused by extension. *Nature*,
713 464(7290), 885–889.
- 714 Moschetti, M., Ritzwoller, M., Lin, F.-C., & Yang, Y. (2010a). Crustal shear wave
715 velocity structure of the western united states inferred from ambient seismic
716 noise and earthquake data. *Journal of Geophysical Research: Solid Earth*,
717 115(B10).
- 718 Moschetti, M., Ritzwoller, M., & Shapiro, N. (2007). Surface wave tomography of
719 the western united states from ambient seismic noise: Rayleigh wave group

- 720 velocity maps. *Geochemistry, Geophysics, Geosystems*, 8(8).
- 721 Pasyanos, M. E., Masters, T. G., Laske, G., & Ma, Z. (2014). Litho1. 0: An updated
722 crust and lithospheric model of the earth. *Journal of Geophysical Research: Solid Earth*, 119(3), 2153–2173.
- 723 Porter, R., Liu, Y., & Holt, W. E. (2016). Lithospheric records of orogeny within the
724 continental us. *Geophysical Research Letters*, 43(1), 144–153.
- 725 Rudnick, R., & Gao, S. (2014). Composition of the continental crust, in Treatise on
726 Geochemistry. Elsevier, San Diego, Calif., 4, 1–51.
- 727 Sambridge, M. (1999). Geophysical inversion with a neighbourhood algorithm—i.
728 searching a parameter space. *Geophysical journal international*, 138(2), 479–
729 494.
- 730 Schaeffer, A., & Lebedev, S. (2015). Global heterogeneity of the lithosphere and
731 underlying mantle: A seismological appraisal based on multimode surface-wave
732 dispersion analysis, shear-velocity tomography, and tectonic regionalization. In
733 *The earth's heterogeneous mantle* (pp. 3–46). Springer.
- 734 Schardong, L., Ferreira, A. M., Berbellini, A., & Sturgeon, W. (2019). The anatomy
735 of uppermost mantle shear-wave speed anomalies in the western us from
736 surface-wave amplification. *Earth and Planetary Science Letters*, 528, 115822.
- 737 Schardong, L., Sturgeon, W., Ferreira, A. M., & Berbellini, A. (2022, November).
738 WUSA surface wave amplification measurements (Schardong et al. 2019).
- 739 Zenodo. Retrieved from <https://doi.org/10.5281/zenodo.7352566> doi:
740 10.5281/zenodo.7352566
- 741 Schellart, W., Stegman, D., Farrington, R., Freeman, J., & Moresi, L. (2010). Cenozoic
742 tectonics of western north america controlled by evolving width of farallon
743 slab. *Science*, 329(5989), 316–319.
- 744 Schmandt, B., & Humphreys, E. (2011). Seismically imaged relict slab from the 55
745 ma siletzia accretion to the northwest united states. *Geology*, 39(2), 175–178.
- 746 Schmandt, B., Lin, F.-C., & Karlstrom, K. E. (2015). Distinct crustal isostasy
747 trends east and west of the rocky mountain front. *Geophysical Research Letters*,
748 42(23), 10–290.
- 749 Shapiro, N. M., Campillo, M., Stehly, L., & Ritzwoller, M. H. (2005). High-
750 resolution surface-wave tomography from ambient seismic noise. *Science*,
751 307(5715), 1615–1618.

- 753 Shen, W., & Ritzwoller, M. H. (2016). Crustal and uppermost mantle structure be-
754 neath the united states. *Journal of Geophysical Research: Solid Earth*, 121(6),
755 4306–4342.
- 756 Shen, W., Ritzwoller, M. H., & Schulte-Pelkum, V. (2013). A 3-d model of the
757 crust and uppermost mantle beneath the central and western us by joint inver-
758 sion of receiver functions and surface wave dispersion. *Journal of Geophysical*
759 *Research: Solid Earth*, 118(1), 262–276.
- 760 Smith, R., Schilly, M., Braile, L., Ansorge, J., Lehman, J., Baker, M., ... Greens-
761 felder, R. (1982). The 1978 yellowstone-eastern snake river plain seismic pro-
762 filing experiment: Crustal structure of the yellowstone region and experiment
763 design. *Journal of Geophysical Research: Solid Earth*, 87(B4), 2583–2596.
- 764 Sparlin, M. A., Braile, L., & Smith, R. B. (1982). Crustal structure of the east-
765 ern snake river plain determined from ray trace modeling of seismic refraction
766 data. *Journal of Geophysical Research: Solid Earth*, 87(B4), 2619–2633.
- 767 Stewart, J. H. (1980). Geology of nevada. *Nevada Bureau of Mines and Geology spe-*
768 *cial publication*, 4, 136.
- 769 Szwilus, W., Afonso, J. C., Ebbing, J., & Mooney, W. D. (2019). Global crustal
770 thickness and velocity structure from geostatistical analysis of seismic data.
771 *Journal of Geophysical Research: Solid Earth*, 124(2), 1626–1652.
- 772 Taylor, S. R., Gerstoft, P., & Fehler, M. C. (2009). Estimating site amplification fac-
773 tors from ambient noise. *Geophysical research letters*, 36(9).
- 774 Tesauro, M., Kaban, M. K., Mooney, W. D., & Cloetingh, S. (2014). Nacr14: A
775 3d model for the crustal structure of the north american continent. *Tectono-*
776 *physics*, 631, 65–86.
- 777 van Heijst, H. J., & Woodhouse, J. (1997). Measuring surface-wave overtone phase
778 velocities using a mode-branch stripping technique. *Geophysical Journal Inter-*
779 *national*, 131(2), 209–230.
- 780 Voronoï, G. (1908). Nouvelles applications des parametres continus a la theorie
781 des forms quadratiques. deuxieme memoire: Recheches sur les parallelloedres
782 primitifs. *J. reine angew. Math.*, 134, 198–287.
- 783 Walker, J. D., Bowers, T. D., Glazner, A. F., Farmer, A., & Carlson, R. W. (2004).
784 Creation of a north american volcanic and plutonic rock database (navdat). In
785 *Geological society of america abstracts with programs* (Vol. 36, p. 9).

- 786 Wessel, P., & Smith, W. H. (1998). New, improved version of generic mapping tools
787 released. *Eos, Transactions American Geophysical Union*, 79(47), 579–579.
- 788 Xie, J., Chu, R., & Yang, Y. (2018). 3-d upper-mantle shear velocity model beneath
789 the contiguous united states based on broadband surface wave from ambient
790 seismic noise. *Pure and Applied Geophysics*, 175(10), 3403–3418.
- 791 Yudistira, T., Paulssen, H., & Trampert, J. (2017). The crustal structure beneath
792 the netherlands derived from ambient seismic noise. *Tectonophysics*, 721, 361–
793 371.
- 794 Zandt, G., Myers, S. C., & Wallace, T. C. (1995). Crust and mantle structure across
795 the basin and range-colorado plateau boundary at 37° n latitude and implica-
796 tions for cenozoic extensional mechanism. *Journal of Geophysical Research:*
797 *Solid Earth*, 100(B6), 10529–10548.